RESEARCH ARTICLE

Improved Direct Torque Control of Induction Motor for Torque Ripple Minimization

TOMAS ESPARZA SOLA [ID]1, **HUANG JEN CHIU** [ID]1, **(Senior Member, IEEE)**,
YU-CHEN LIU [ID]2, **(Senior Member, IEEE), AND ARIEF NOOR RAHMAN** [ID]3

1 Department of Electronic and Computer Engineering, National Taiwan University of Science and Technology, Taipei 10607, Taiwan
2 Department of Electrical Engineering, National Ilan University, Yilan 260, Taiwan
3 Pegatron Corporation, Automotive Business Unit, Taoyuan 333, Taiwan

Corresponding author: Tomas Esparza Sola (esparzsol@gmail.com)

ABSTRACT A new direct torque control (DTC) method of an induction motor (IM) which minimizes torque ripple (T_{ripp}) while preserving all the conventional DTC advantages is presented in this paper. Large T_{ripp} and current ripple are the main drawbacks of the conventional DTC. To address this problem, this paper gives a qualitative analysis of the main T_{ripp} sources of the conventional DTC. A novel strategy to reduce T_{ripp} in the constant T and in the field weakening (FW) regions is proposed. The performance of the proposed method is evaluated and compared with a recently published method that aims for the same goals that are pursued in this paper, as well as with the conventional DTC. The analysis has been carried out on the basis of the results obtained by theoretical analysis and hardware implementation.

INDEX TERMS Direct torque control, torque ripple, dynamic response, acceleration process.

I. INTRODUCTION

Good dynamic response of an IM is vital for most of the industrial applications. Traditionally, scalar control schemes (Volts by Hertz) were typically implemented for IM. Said schemes, however, despite having a good steady-state performance, have a poor dynamic response [1], [2]. Hence, these schemes can be found in low-performance drives such as pumps or fans. On the other hand, when a higher performance is required, vector control is usually the preferred choice. Vector control allows operating an IM in an almost identical manner as a separately excited DC machine with detached control of torque and flux [3].

The conventional DTC scheme proposed by Takahashi [4] provides instantaneous electromagnetic torque (T) response, and since it does not require coordinate transformations, it is simpler compared to the field-oriented control. However, this algorithm has important drawbacks, such as high torque ripple (T_{ripp}), varying switching frequency and high current THD [5], [8]. Constant switching frequency has been achieved to a certain extent by different publications. One

of the modified DTC algorithms to attain constant switching frequency is known as space vector modulated direct torque control (SVM-DTC). It is commonly found in the literature that the closed-loop control of said algorithm is made by means of PI controllers or more advanced strategies, such as predictive or neuro-fuzzy controllers [9], [12]. An advanced DTC scheme with feedback linearization applying sliding mode control is presented in [11]. Another DTC-based algorithm that achieves nearly constant switching frequency via adaptive hysteresis bands is proposed in [13]. The constant switching frequency DTC strategy proposed in [14] implements space vector pulse width modulation by calculating in real-time the required reference voltage vector. These papers have mainly focused on the constant switching frequency regulation; thus, these methods have not shown a large improvement in reducing instantaneous T_{ripp}. Moreover, these strategies require extensive real-time calculations, increasing the complexity compared to the conventional DTC algorithm.

Several T_{ripp} reduction strategies that consist of multilevel inverters or double-inverter-fed motor drives can be found in the literature [15], [23]. However, the hardware complexity is substantially increased in these architectures.

Furthermore, [16], [20], and [21] utilize PI controllers to regulate torque and flux. As a result, the dynamic response is worsened compared to the conventional DTC. Reference [16] also implements fuzzy-based control, increasing the computational requirements.

Model Predictive Control (MPC) is also commonly found in the literature [24], [26] as a strategy to reduce T_{ripp}. However, MPC-based strategies have important drawbacks. First of all, the selection process of the best switching state. The cost function is calculated for all possible combinations of the switching states. As the number of switching devices increases, the number of switching options increases exponentially, which makes the real-time implementation of the MPC strategy challenging [27], [28], [29]. Furthermore, predictive controllers are, by definition a model-based control technique and its formulation relies on the knowledge of the electrical parameters of the machine [27]. However, the direct use of system model for selecting the optimal control actions make predictive methods prone to changes in their performance when facing modeling errors or parameter variations. Therefore, the influence of errors in the prediction model remains as a major concern. Moreover, the prediction error is not only determined by parametric mismatch but also by the instantaneous values of load current and inverter output voltage [30], [31]. In order to ensure adequate performance, the effects of parameters mismatch in MPC have been assessed in in the literature [29], [32], [33]. Consequently, these parameter identification algorithms further increase the already heavy computational burden of the MPC-based methods. An example that follows this approach can be found in [34]. Additionally, MPC architectures require to compensate the time delay caused by the data processing [35]. As a result, the computational burden of the MPC-based methods is prohibitively heavy for most of the standard industrial microcontroller boards.

The T_{ripp} minimization algorithms proposed in [36] and [37] are highly dependent on parameters. Thus, as happens for MPC-based architectures, online parameter identification algorithms have to be implemented. Moreover, the method proposed in [36] requires complex real-time calculations. For the case of [37], T_{ripp} is reduced in steady state but not during transients.

Another approach to reduce T_{ripp} is found in [38]. In this method, the stator flux magnitude $\left(\left| \overrightarrow{\lambda_s} \right| \right)$ and T are controlled in separate sampling intervals, each at a time. Hence, a voltage vector that potentially could increase T is selected once every two sampling intervals. As it is shown in section III, this modus operandi causes severe T drops in the high-speed region, contributing to the increase of T_{ripp}. Furthermore, the control method proposed in the said article is based on the premise that $\left| \overrightarrow{\lambda_s} \right|$ ripple reduction is as important as T_{ripp} reduction. However, as it is stated in [39], T_{ripp} creates more severe consequences, such as acoustic noise, vibration, and current THD.

Advanced control algorithms are also found in the literature as an alternative to reduce T_{ripp}. Sliding-mode control and feedback linearization are implemented in [11]. This method requires extensive computational power and is limited to the linear operation region.

A class of DTC schemes based on the concept of virtual vectors is proposed in [40]. In these schemes, conventional DTC is modified to reduce T_{ripp} by increasing the number of space voltage vectors that can be selected. The method proposed in [40] effectively reduces T_{ripp} in the low and medium speed ranges with a computational burden similar to the method that we propose. However, important drawbacks that are further discussed and compared to the performance of the method proposed in this paper, are also introduced.

Even though the efforts of the aforementioned papers have rendered the conventional DTC certain improvements in some aspects, they tend to do that by sacrificing one or more characteristics that make this method extensively implemented. These features are: simple algorithm with low computational cost, fast T dynamic response, maximum utilization of the DC bus capability, and maximum operating range of the constant T region. Therefore, the contributions of this article are listed as follows:

1) A novel DTC algorithm for an IM to effectively minimize T_{ripp} in the constant T and in the FW regions is proposed. This method is capable of preserving the totality of the positive attributes of the conventional DTC previously mentioned. Based on the conventional DTC, the minimum magnitude space voltage vector to provide the desired T response for any load condition when $T < T^*$ is obtained. In order to enhance the T_{ripp} reduction in the medium and high-speed regions, an additional strategy based on limiting T drop when $T > T^*$ is also implemented in these regions.

2) Since T drop is limited, the acceleration process is improved, making this paper capable to provide faster acceleration than the conventional DTC.

3) An analysis of the T_{ripp} sources in the conventional DTC is developed.

4) A detailed performance comparison of the proposed method, the approach developed in [40], and the conventional DTC is presented.

The remainder of this paper is arranged as follows. Section II describes the T production equations for an IM. Section III is an explanation of conventional DTC and its T_{ripp} sources. Section IV is a brief description of the method presented in [40] and its drawbacks. In Section V, a novel T_{ripp} minimization algorithm is proposed and analyzed. Section VI presents the stator flux estimator that is implemented in this study. Furthermore, the calculation of the reference stator flux magnitude $\left(\lambda_s^* \right)$ is explained in detail. The experimental results and comparative analysis are shown in Section VII.
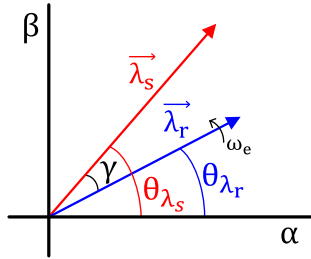
FIGURE 1. Stator and rotor flux vectors.

II. INDUCTION MOTOR TORQUE EQUATIONS

In this section, IM T equations are developed. From [41] and with a few assumptions that are explained below, T equations are adapted to apply them to the analysis that takes place in this dissertation, as well as on the proposed method.

For an IM, T can be expressed as [41]:

$$T = \frac{3}{2} P_P \frac{L_m}{L_s L_r - L_m^2} \left| \overrightarrow{\lambda_s} \right| \left| \overrightarrow{\lambda_r} \right| \sin(\gamma) \quad (1)$$

where P_P is the number of poles, $\left| \overrightarrow{\lambda_s} \right|$ and $\left| \overrightarrow{\lambda_r} \right|$ are the stator and rotor flux magnitudes, respectively, γ is the angle between stator flux $\left(\overrightarrow{\lambda_s} \right)$ and rotor flux $\left(\overrightarrow{\lambda_r} \right)$, as it is shown in Fig. 1. L_s is the stator inductance, L_r is the rotor inductance and L_m is the magnetizing inductance.

For constant $\left| \overrightarrow{\lambda_s} \right|$ and $\left| \overrightarrow{\lambda_r} \right|$, the change in torque ($\Delta T$) is almost proportional to the rate of change of γ.

$$\Delta T = \frac{3}{2} P_P \frac{L_m}{L_s L_r - L_m^2} \left| \overrightarrow{\lambda_s} \right| \left| \overrightarrow{\lambda_r} \right| \sin(\Delta \gamma) \quad (2)$$

Assuming that in one sampling period (T_s), $\Delta \gamma$ is small, ΔT can be expressed as:

$$\Delta T = K_T \cdot \Delta \gamma \quad (3)$$

where $K_T = \frac{3}{2} P_P \frac{L_m}{L_s L_r - L_m^2} \left| \overrightarrow{\lambda_s} \right| \left| \overrightarrow{\lambda_r} \right|$

Given its slow dynamic response, the rotational speed of $\overrightarrow{\lambda_r}$ can be considered constant and equal to ω_e [41], as it is indicated in Fig. 1. Hence, the change in the rotor flux angle $\left(\Delta \theta_{\lambda_r} \right)$ can be expressed as:

$$\Delta \theta_{\lambda_r} = \omega_e \cdot T_s \quad (4)$$

Thus, ΔT is obtained:

$$\Delta T = K_T \cdot \left(\Delta \theta_{\lambda_s} - \omega_e \cdot T_s \right) \quad (5)$$

III. CONVENTIONAL DTC PRINCIPLES

The conventional DTC scheme [4] has the following working principle, as shown in Fig. 2a. The error between T and the reference torque (T^*) is the input of the three-level hysteresis comparator that can be found in Fig. 2c. Similarly, the error between $\left| \overrightarrow{\lambda_s} \right|$ and λ_s^* is the input of the two-level hysteresis comparator that can be found in Fig. 2b.

The digitized output of the flux and torque hysteretic controllers, as well as the stator flux position sector, are the inputs
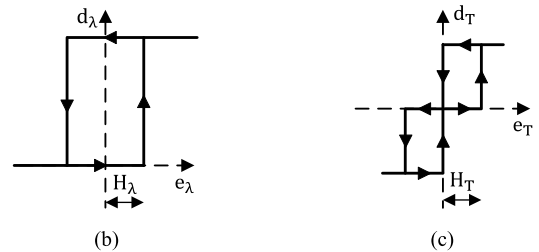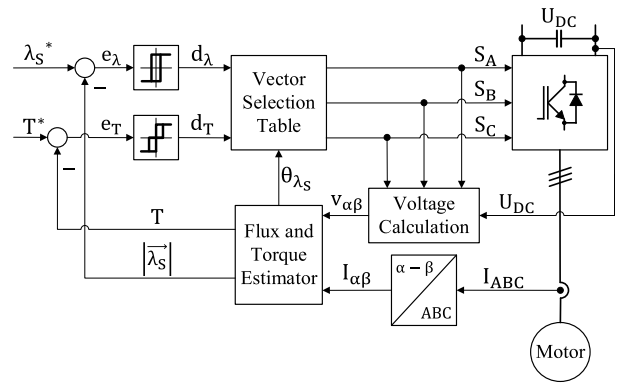

FIGURE 2. Conventional DTC principle: (a) Control scheme; (b) Flux hysteretic cycle; (c) Torque hysteretic cycle.

TABLE 1. Conventional DTC Optimum Switching Table.

d_ψ	d_T	Sector 1	Sector 2	Sector 3	Sector 4	Sector 5	Sector 6
	1	$\overrightarrow{U_2}$	$\overrightarrow{U_3}$	$\overrightarrow{U_4}$	$\overrightarrow{U_5}$	$\overrightarrow{U_6}$	$\overrightarrow{U_1}$
1	0	$\overrightarrow{U_7}$	$\overrightarrow{U_0}$	$\overrightarrow{U_7}$	$\overrightarrow{U_0}$	$\overrightarrow{U_7}$	$\overrightarrow{U_0}$
	-1	$\overrightarrow{U_6}$	$\overrightarrow{U_1}$	$\overrightarrow{U_2}$	$\overrightarrow{U_3}$	$\overrightarrow{U_4}$	$\overrightarrow{U_5}$
	1	$\overrightarrow{U_3}$	$\overrightarrow{U_4}$	$\overrightarrow{U_5}$	$\overrightarrow{U_6}$	$\overrightarrow{U_1}$	$\overrightarrow{U_2}$
0	0	$\overrightarrow{U_0}$	$\overrightarrow{U_7}$	$\overrightarrow{U_0}$	$\overrightarrow{U_7}$	$\overrightarrow{U_0}$	$\overrightarrow{U_7}$
	-1	$\overrightarrow{U_5}$	$\overrightarrow{U_6}$	$\overrightarrow{U_1}$	$\overrightarrow{U_2}$	$\overrightarrow{U_3}$	$\overrightarrow{U_4}$

to select the appropriate actual voltage vector $\left(\overrightarrow{U_{actual}} \right)$ from the switching table, which can be found in Table 1. The pulses to control the inverter power switches (S_A, S_B, and S_C) are generated based on the selection table.

As shown in Fig. 3, for the conventional DTC method, the plane is divided into six sectors. Taking sector 1 as an example, $\overrightarrow{U_1}$, $\overrightarrow{U_2}$ or $\overrightarrow{U_6}$ can be selected to increase $\left| \overrightarrow{\lambda_s} \right|$. Conversely, a decrease can be obtained by selecting $\overrightarrow{U_3}$, $\overrightarrow{U_4}$ or $\overrightarrow{U_5}$. To increase T, $\overrightarrow{U_2}$, $\overrightarrow{U_3}$ or $\overrightarrow{U_4}$ can be selected. A reduction in T can be obtained by selecting $\overrightarrow{U_1}$, $\overrightarrow{U_5}$ or $\overrightarrow{U_6}$.

A. ANALYSIS OF T_{ripp} SOURCES IN THE CONVENTIONAL DTC

At low speed, during one T_s, $\Delta \theta_{\lambda_r} \approx 0$ and $\Delta \gamma \approx \Delta \theta_{\lambda_s}$. Hence, from (5), ΔT can be expressed as

$$\Delta T \approx K_T \cdot \Delta \theta_{\lambda_s} \quad (6)$$
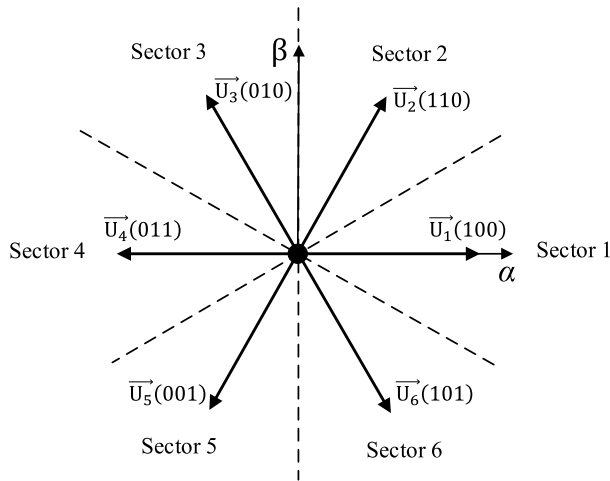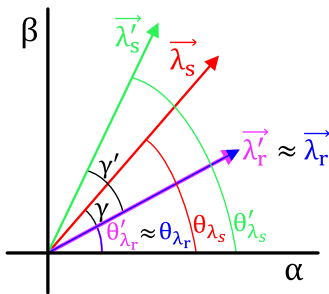
FIGURE 3. Actual voltage vectors in conventional DTC.

FIGURE 4. Excessive torque rise at low speed.

Thus, if $\overrightarrow{U_{actual}}$ is applied, $\Delta\gamma$ will be very large, and so ΔT. This situation is illustrated in Fig. 4. Note that from now on, the apostrophe in the figures means *next sampled value*. It is written instead of $(k+1)$ to save space.

For conventional DTC, when T needs to be decreased, the approach is to apply a zero-voltage vector $\left(\overrightarrow{U_Z}\right)$. Applying such a vector stops $\overrightarrow{\lambda_s}$. Accordingly, $\Delta\gamma$ is reduced and so T. In this situation, (5) can be rewritten as:

$$\Delta T \approx -K_T \cdot T_s \cdot \omega_e \qquad (7)$$

At low speed, this is a correct approach, T is slowly decreased without contributing to T_{ripp} generation. However, at high speed, during one T_s, $\Delta\theta_{\lambda_r}$ is very large. Hence, given that $\Delta\theta_{\lambda_s} \approx 0$ and $\Delta\gamma \approx -\Delta\theta_{\lambda_r}$, T is excessively decreased. This situation is illustrated in Fig. 9(a).

IV. VIRTUAL SPACE VECTOR-BASED DIRECT TORQUE CONTROL METHOD

In this section, a recently published article [40] that aims for the same goal as this dissertation is examined. In addition, its weaknesses related to the method that we propose are briefly discussed. The said article presents different DTC schemes based on the concept of virtual voltage space vectors. The first scheme is almost identical to the conventional DTC. Nevertheless, it utilizes six virtual voltage vectors $\left(\overrightarrow{U_{virtual}}\right)$
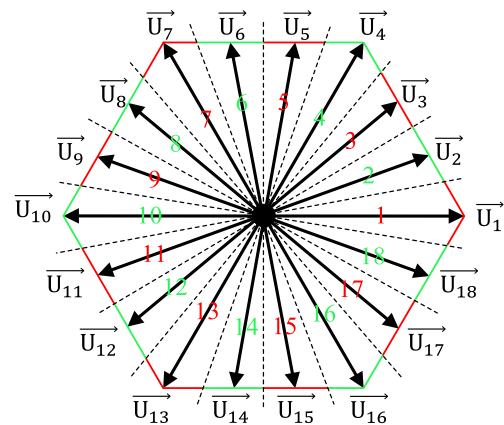

FIGURE 5. Sector division in direct torque control with eighteen sectors.

instead of the six $\overrightarrow{U_{actual}}$ characteristic of conventional DTC. The magnitude of the virtual vectors $\left(\left|\overrightarrow{U_{virtual}}\right|\right)$ is smaller than the magnitude of the actual voltage vectors $\left(\left|\overrightarrow{U_{actual}}\right|\right)$. Thus, T response is degraded, and the maximum attainable speed is limited. Additionally, to synthesize $\overrightarrow{U_{virtual}}$, it is necessary to switch the two adjacent $\overrightarrow{U_{actual}}$, increasing the switching losses with respect to the conventional DTC. As a consequence, the first scheme does not provide improvements to the conventional DTC and substantial drawbacks are introduced. The second and third structures use a combination of $\overrightarrow{U_{virtual}}$ and $\overrightarrow{U_{actual}}$. A T_{ripp} reduction is achieved by these two schemes at the expense of losing important attributes of the conventional DTC algorithm. Among the proposed structures, the highest T_{ripp} reduction is obtained for the scheme that utilizes eighteen sectors and a total of twenty voltage vectors. These vectors are composed of six $\overrightarrow{U_{actual}}$, twelve $\overrightarrow{U_{virtual}}$, and two $\overrightarrow{U_Z}$. Hence, said scheme is going to be used for comparison. $\overrightarrow{U_{actual}}$ are the same as in the conventional DTC. Thus, $\left|\overrightarrow{U_{actual}}\right| = 2/3 \cdot U_{DC}$ but $\left|\overrightarrow{U_{virtual}}\right| \approx 0.586 \cdot U_{DC}$.

The space vector distribution of this method can be seen in Fig. 5.

Compared to the method that we propose, this strategy to reduce T_{ripp} has several disadvantages. First of all, when T has to be increased, the full voltage vector is applied, even for a small T error. Hence, for low and medium-speed regions, T rises excessively, producing high T_{ripp}. Secondly, the algorithm relies on $\overrightarrow{U_Z}$ to reduce T, creating severe T drops at high speeds. Furthermore, this method has a limited maximum attainable speed. Moreover, since sectors are narrower, flux angle estimation needs to be more accurate. These disadvantages will be proved and further discussed in section VI.

V. PROPOSED TORQUE RIPPLE MINIMIZATION ALGORITHM

In this section, the proposed T_{ripp} minimization algorithm is explained. A T_{ripp} reduction strategy is implemented both
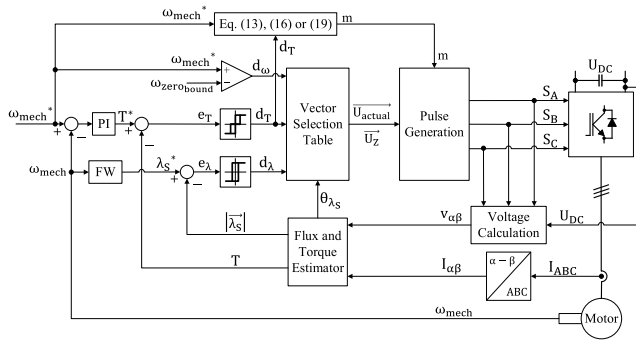
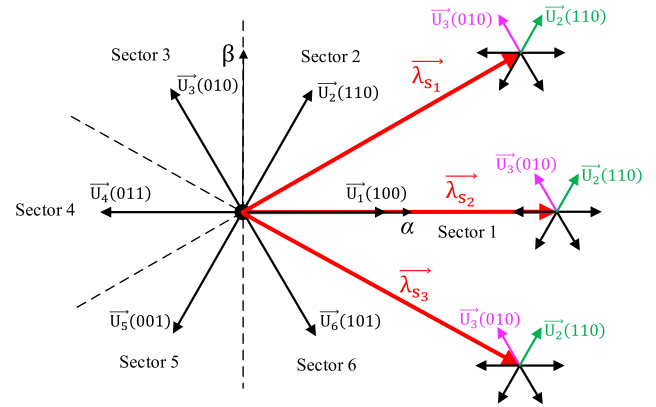**FIGURE 6.** Control diagram of the proposed torque ripple minimization algorithm.

FIGURE 7. Torque generation for different θ_{λ_s}.

FIGURE 8. Stator flux vector when torque needs to be increased: (a) Stator flux module is increased; (b) Stator flux module is decreased.

when $T<T^*$ and when $T>T^*$. For the case where $T<T^*$, the minimum magnitude active voltage vector $\left(\overrightarrow{U_{active}}\right)$ that provides a good dynamic T response for the whole load range is obtained. Conversely, the T_{ripp} minimization strategy for the situation where $T>T^*$, is based on limiting the T drop. This strategy, as explained in section III, is the main source of T_{ripp} in the medium and high-speed regions.

The overall control diagram of the proposed T_{ripp} minimization algorithm is depicted in Fig. 6. It can be seen that λ_s^* is generated by the FW block and T^* is generated by an external speed control loop. Due to the fact that its proven reliability and easiness of implementation, a PI regulator is chosen to control the speed. However, if the reader of this article feels the necessity to optimize the speed response and can afford the increment of the computational burden, the speed controller could be designed according to more advanced techniques, such as sliding mode control [44]. A detailed explanation of the control diagram presented in Fig. 6 and the T_{ripp} minimization strategies when $T<T^*$ and when $T>T^*$ are described as follows.
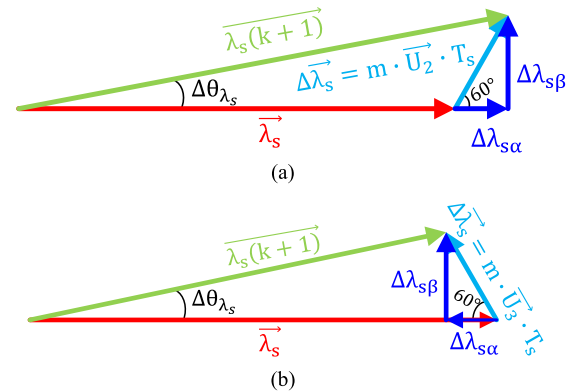
A. MINIMUM T_{ripp} ALGORITHM WHEN $T<T^*$

In order to obtain $\overrightarrow{U_{active}}$, a simple ω_{mech}-dependent equation shall be obtained as follows.

Assuming that $\overrightarrow{\lambda_s}$ is in sector 1 and both T and $\left|\overrightarrow{\lambda_s}\right|$ have to be increased, based on Table 1, $\overrightarrow{U_2}$ should be chosen. However, if T needs to be increased but $\left|\overrightarrow{\lambda_s}\right|$ has to be decreased, $\overrightarrow{U_3}$ should be chosen instead. Fig. 7 shows three different scenarios corresponding to three different θ_{λ_s}. For the case where $\left|\overrightarrow{\lambda_s}\right|$ has to be increased, $\overrightarrow{U_2}$ is perpendicular to $\overrightarrow{\lambda_{s_3}}$. Hence, it is in this specific moment when T production reaches the maximum. Contrarily, the minimum T production corresponds to $\overrightarrow{\lambda_s}=\overrightarrow{\lambda_{s_1}}$. It is easily deducible that the average T production that $\overrightarrow{U_2}$ generates over the whole sector 1 corresponds to the situation where $\overrightarrow{\lambda_s}=\overrightarrow{\lambda_{s_2}}$, which coincides with the middle of sector 1. On the other hand, for the case where $\left|\overrightarrow{\lambda_s}\right|$ has to be decreased, the maximum and minimum T production correspond to $\overrightarrow{\lambda_s}=\overrightarrow{\lambda_{s_1}}$ and

$\overrightarrow{\lambda_s}=\overrightarrow{\lambda_{s_3}}$, respectively. In the same fashion as for $\overrightarrow{U_2}$, the average T production that $\overrightarrow{U_3}$ generates over the whole sector 1 corresponds to the situation where $\overrightarrow{\lambda_s}=\overrightarrow{\lambda_{s_2}}$.

A graphical representation of $\overrightarrow{\lambda_s}$ being in the middle of sector 1 when both T and $\left|\overrightarrow{\lambda_s}\right|$ have to be increased is shown in Fig. 8(a). Equally, Fig. 8(b) illustrates the circumstance where T has to be increased but $\left|\overrightarrow{\lambda_s}\right|$ decreased.

In Fig. 8, m is the ratio of $\left|\overrightarrow{U_{actual}}\right|$ that is applied. It goes from 0 to 1. For instance, for the situation depicted in Fig. 8(a), if $m=0.5$, $\overrightarrow{U_{active}}||\overrightarrow{U_2}$ but $\left|\overrightarrow{U_{active}}\right|=0.5\cdot\left|\overrightarrow{U_2}\right|$. In Fig. 8, $\left|\overrightarrow{U_2}\right|=\left|\overrightarrow{U_3}\right|=\left|\overrightarrow{U_{actual}}\right|=(2/3)\cdot U_{DC}$.

For the two situations depicted in Fig. 8, it happens that for small values of $\Delta\theta_{\lambda_s}$, the following approximations can be done:

$$\left|\overrightarrow{\lambda_s}\right|+\Delta\lambda_{s\alpha}\approx\left|\overrightarrow{\lambda_s(k+1)}\right|\approx\lambda_s^* \tag{8}$$

$$\Delta\lambda_{s\beta}=m\cdot\left|\overrightarrow{U_{actual}}\right|\cdot\sin(60°)\cdot T_s$$
$$\approx 2\cdot\lambda_s^*\cdot\sin\left(\frac{\Delta\theta_{\lambda_s}}{2}\right)\approx\lambda_s^*\cdot\Delta\theta_{\lambda_s} \tag{9}$$

Combining (5) and (9) the following equation is obtained:

$$\frac{\Delta T}{K_T} + \omega_e \cdot T_s = \frac{m \cdot \left| \overrightarrow{U_{actual}} \right| \cdot \sqrt{3} \cdot T_s}{2 \cdot \lambda_s^*} \quad (10)$$

Since the goal of the method that we propose is to reduce T_{ripp} by applying the minimum $\left| \overrightarrow{U_{active}} \right|$ that will simultaneously provide a good T response for the whole load range, the worst-case scenario is when the motor is working at full load. For this condition, the slip speed (ω_{sl}) is equal to its maximum value. $\omega_{sl_{max}}$ is calculated based on [42]. If a good T response is guaranteed for such a condition, it is straightforward that a good response is going to be provided for the whole load range. Thus, for full-load conditions, (10) can be rewritten as

$$\frac{\Delta T}{K_T} + \left(\omega_{sl_{max}} + P_P \cdot \omega_{mech} \right) \cdot T_s = \frac{m \cdot \left| \overrightarrow{U_{actual}} \right| \cdot \sqrt{3} \cdot T_s}{2 \cdot \lambda_s^*} \quad (11)$$

Isolating m

$$m = \frac{2 \cdot \lambda_s^*}{\left| \overrightarrow{U_{actual}} \right| \cdot \sqrt{3}} \cdot \left(\frac{\Delta T}{K_T \cdot T_s} + \omega_{sl_{max}} + P_P \cdot \omega_{mech} \right) \quad (12)$$

Replacing $\left| \overrightarrow{U_{actual}} \right|$ for its value and ΔT for $\Delta T_{increase}$, which is the minimum T rise in one T_s required to have a good T dynamic response at full-load conditions. $\Delta T_{increase}$ is obtained according to [39].

$$m = \frac{\sqrt{3} \cdot \lambda_s^*}{U_{DC}} \cdot \left(\frac{\Delta T_{increase}}{K_T \cdot T_s} + \omega_{sl_{max}} + P_P \cdot \omega_{mech} \right) \quad (13)$$

Since the only variable in (13) is ω_{mech}, a simple first-order equation has been obtained. Once the point where $m = 1$ has been reached, $\left| \overrightarrow{U_{active}} \right| = \left| \overrightarrow{U_{actual}} \right|$, and the algorithm behaves as conventional DTC. The ω_{mech} value at which $m = 1$ is referred as the mechanical base speed $\left(\omega_{mech_{base}} \right)$. The maximum mechanical speed $\left(\omega_{mech_{max}} \right)$ that can be reached with this method (for full-load conditions) corresponds to the case where T cannot be further increased. In other words, $\Delta T_{increase} = 0$. For this situation, $\Delta \theta_{\lambda_s} = \Delta \theta_{\lambda_r}$ and $\Delta \gamma = 0$. Applying said conditions in (13), $\omega_{mech_{max}}$ is obtained

$$\omega_{mech_{max}} = \frac{1}{P_P} \cdot \left(\frac{U_{DC}}{\sqrt{3} \cdot \lambda_s^*} - \omega_{sl_{max}} \right) \quad (14)$$

B. MINIMUM T_{ripp} ALGORITHM WHEN $T > T^*$

Equation (7) shows that when $\overrightarrow{U_Z}$ is applied, the higher ω_e, the higher the T reduction. Hence, it is clear that at some point, for a high value of ω_e, T reduction when said vector is applied is going to be excessively large, contributing to the growth of T_{ripp}. After this point, a wiser strategy to reduce T is to apply a small $\left| \overrightarrow{U_{active}} \right|$ which will produce a modest $\Delta \theta_{\lambda_s}$. To guarantee that T is reduced, it must be ensured that $\Delta \theta_{\lambda_s} < \Delta \theta_{\lambda_r}$ for all conditions. Due to the fact that
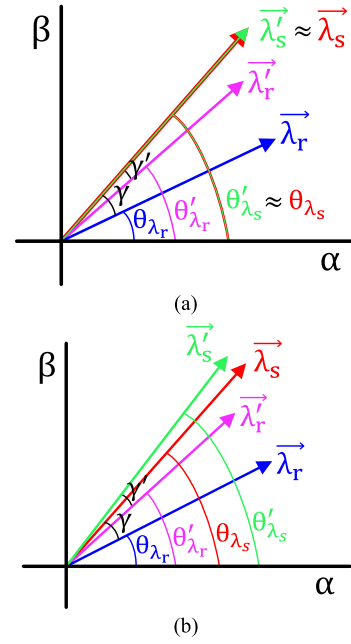

FIGURE 9. Torque reduction at high speed: (a) Zero-voltage vector is applied; (b) Small magnitude active voltage vector is applied.

the smallest T reduction happens for no-load conditions, the algorithm is going to be developed for said circumstances. Fig. 9(b) shows how a negative $\Delta \gamma$ and thus, a T reduction can be obtained by applying $\overrightarrow{U_{active}}$. Since $|\Delta \gamma|$ in Fig. 9(b) is smaller than in Fig. 9(a), T reduction and hence, T_{ripp} are smaller than for the case where $\overrightarrow{U_Z}$ is applied.

To guarantee the controllability of the system, the parameter $\Delta T_{decrease}$ is introduced. This parameter corresponds to the minimum T reduction in one T_s that is necessary to provide when $\overrightarrow{U_{active}}$ is applied. As for $\Delta T_{increase}$, $\Delta T_{decrease}$ can be also obtained according to [39]. Note that since $\Delta T_{decrease}$ indicates a T reduction, such a parameter has a negative value.

As mentioned before, T reduction when $\overrightarrow{U_Z}$ is applied escalates with ω_e. For no-load conditions, $\omega_e = P_P \cdot \omega_{mech}$. Hence, $\omega_{zero_{bound}}$ is going to be defined as the value of ω_{mech} for which the T reduction equals $\Delta T_{decrease}$ when $\overrightarrow{U_Z}$ is applied. If $\omega_{mech} < \omega_{zero_{bound}}$, T will be reduced by applying $\overrightarrow{U_Z}$. On the contrary, if $\omega_{mech} > \omega_{zero_{bound}}$, T will be reduced by applying $\overrightarrow{U_{active}}$. The election procedure of the voltage vector that will be applied is presented in the block diagram shown in Fig. 10.

From (7), if ω_e is replaced with $P_P \cdot \omega_{mech}$, and ΔT with $\Delta T_{decrease}$, $\omega_{zero_{bound}}$ is obtained

$$\omega_{zero_{bound}} = -\frac{\Delta T_{decrease}}{K_T \cdot P_P \cdot T_s} \quad (15)$$

After $\omega_{zero_{bound}}$, $\left| \overrightarrow{U_{active}} \right|$ to obtain a T reduction that matches $\Delta T_{decrease}$ (for no-load condition) is obtained as follows. Said $\overrightarrow{U_{active}}$ is based on the same $\overrightarrow{U_{actual}}$ that, according to Table 1, would increase T. Thus, the situation is the same
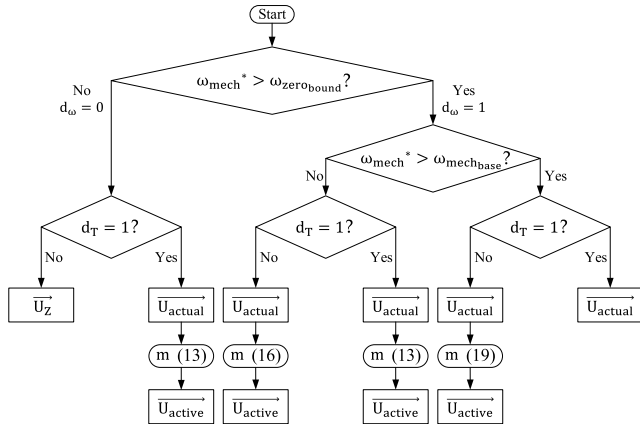
FIGURE 10. Voltage vector election procedure.

as the one depicted in Fig. 8. However, in this case $\Delta\theta_{\lambda_s} < \Delta\theta_{\lambda_r}$. Hence from (10), if ω_e is replaced with $P_P \cdot \omega_{mech}$, ΔT with $\Delta T_{decrease}$ and, m is isolated, the following equation is obtained

$$m = \frac{\sqrt{3} \cdot \lambda_s^*}{U_{DC}} \cdot \left(\frac{\Delta T_{decrease}}{K_T \cdot T_s} + P_P \cdot \omega_{mech} \right) \quad (16)$$

C. MINIMUM T_{ripp} ALGORITHM IN THE FLUX WEAKENING REGION

As it was previously mentioned, after $\omega_{mech_{base}}$, for the case where $T < T^*$, it happens that $m = 1$. Thus, $\overrightarrow{U_{active}} = \overrightarrow{U_{actual}}$ and the T_{ripp} minimization algorithm does not require further consideration. On the other hand, the situation where $T > T^*$ in the FW region requires more detailed examination.

Following the same fashion as for the constant T region, the algorithm is developed for no-load condition, which is the worst-case scenario when $T > T^*$. For this situation, the magnitude of the rotor current $\left(\left| \overrightarrow{I_r} \right| \right)$ is very small and can be considered to be zero. As a result, $\left| \overrightarrow{\lambda_r} \right|$ can be approximated as

$$\left| \overrightarrow{\lambda_r} \right| \approx \frac{L_m}{L_s} \cdot \left| \overrightarrow{\lambda_s} \right| \quad (17)$$

Hence, considering that $\lambda_s^* \approx \left| \overrightarrow{\lambda_s} \right|$, K_T can be rewritten as

$$K_T = K_L \cdot \lambda_s^{*2} \quad (18)$$

where $K_L = \frac{3}{2} P_P \frac{L_m^2}{L_s \cdot (L_s L_r - L_m^2)}$

Accordingly, combining (16), (18), and (23), the equation for m when $T > T^*$ in the FW region is obtained as

$$m = \frac{\sqrt{3}}{U_{DC}} \cdot \left(\frac{\Delta T_{decrease}}{K_L \cdot T_s \cdot \lambda_s^{max} \cdot \omega_{mech_{base}}} \right.$$
$$\left. \cdot \omega_{mech} + P_P \cdot \lambda_s^{max} \cdot \omega_{mech_{base}} \right) \quad (19)$$

As happened for (13) and (16), a simple ω_{mech}-dependent first-order equation has been obtained.

In the FW region, K_T is reduced as the speed increases. Thus, as it can be seen in (3), $|\Delta T|$ decreases along with the K_T reduction, both when $T < T^*$ and when $T > T^*$. In other words, T increment, as well as T reduction are slower in the FW region. As a result, when $T > T^*$ in this region, m is reduced as the speed increases, in a manner contrary to what happened for the constant T region. This phenomenon is graphically shown in Fig. 14.

D. $\overrightarrow{U_{active}}$ GENERATION

In the proposed algorithm, $\overrightarrow{U_{active}}$ can be synthesized by only switching one leg of semiconductors every T_s. Thus, switching losses are reduced to a minimum. $\overrightarrow{U_{active}}$ is generated by applying one of the six $\overrightarrow{U_{actual}}$ for a percentage of T_s (defined by m) and $\overrightarrow{U_Z}$ for the remaining time. If $\overrightarrow{U_{active}}$ is based on $\overrightarrow{U_1}$, $\overrightarrow{U_3}$ or $\overrightarrow{U_5}$, the remaining time is going to be completed with $\overrightarrow{U_Z} = \overrightarrow{U_0}$ (0, 0, 0). On the other hand, if $\overrightarrow{U_{active}}$ is based on $\overrightarrow{U_2}$, $\overrightarrow{U_4}$ or $\overrightarrow{U_6}$, it is to be completed with $\overrightarrow{U_Z} = \overrightarrow{U_7}$ (1, 1, 1). The semiconductors that are not switching will be set high or low for the whole cycle. The switching sequence of the three high-side semiconductors is shown in Table 2. The three low-side semiconductors are complementary to the high-side ones.

The semiconductor that switches within one T_s will be modulated with a sawtooth carrier to insert the corresponding $\overrightarrow{U_Z}$, as it is depicted in Fig. 11.

VI. STATOR FLUX ESTIMATION AND λ_s^* CALCULATION

In this section, the stator flux estimator that is implemented to obtain $\left| \overrightarrow{\lambda_s} \right|$ and θ_{λ_s} is presented. Furthermore, the calculation of λ_s^*, both in the constant T and FW regions is explained in detail.

A. λ_s^* CALCULATION IN THE CONSTANT T REGION

In the constant T region, $\left| \overrightarrow{\lambda_s} \right|$ is normally held at its rated value henceforth defined as λ_s^{max}. Maintaining maximum $\left| \overrightarrow{\lambda_s} \right|$ level is beneficial because it allows the user to have the flexibility to set T between zero and maximum value without the need to adjust $\left| \overrightarrow{\lambda_r} \right|$, which is governed by a large time constant L_r / R_r. If the flux levels are held constant, any torque step will be only dictated by the time needed to change γ. Accordingly, λ_s^{max} can be calculated as [45]

$$\lambda_s^{max} \approx \frac{V_{s_{rated}}}{\omega_{e_{rated}}} \quad (20)$$

where $V_{s_{rated}}$ and $\omega_{e_{rated}}$ are the rated (peak) voltage and rated frequency of the IM, respectively.

On the other hand, for motors without torque-producing current flow in the rotor, such as switched reluctance motors, the performance can be improved by adjusting the flux linkage according to the T variation demand, as it is proposed in [46].

TABLE 2. Switching Sequence for Minimum Switching Losses.

$\overrightarrow{U_{active}}$ based on:	S_1	S_2	S_3
$\overrightarrow{U_1}$	ON → OFF	OFF	OFF
$\overrightarrow{U_2}$	ON	ON	OFF → ON
$\overrightarrow{U_3}$	OFF	ON → OFF	OFF
$\overrightarrow{U_4}$	OFF → ON	ON	ON
$\overrightarrow{U_5}$	OFF	OFF	ON → OFF
$\overrightarrow{U_6}$	ON	OFF → ON	ON
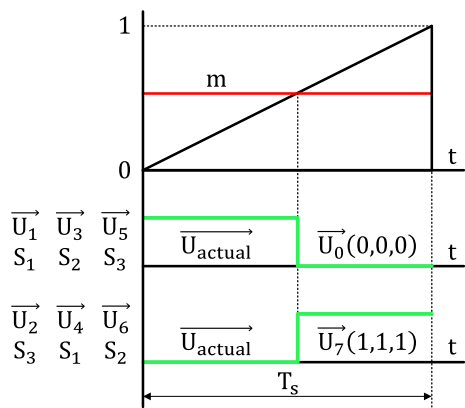
FIGURE 11. $\overrightarrow{U_{active}}$ generation.

B. λ_s^* CALCULATION IN THE FW REGION

In order to allow the operation of the system over the rated speed, $\left|\overrightarrow{\lambda_s}\right|$ has to be decreased. The reason is to limit the back-EMF to a suitable level despite the increase in the speed.

In the FW region, the magnitude of the stator voltage $\left(\left|\overrightarrow{V_s}\right|\right)$ can be approximated as [47]

$$\left|\overrightarrow{V_s}\right| = \omega_e \cdot \left|\overrightarrow{\lambda_s}\right| \tag{21}$$

Thus, in the FW region, λ_s^* can be obtained as

$$\lambda_s^* = \lambda_s^{max} \cdot \frac{\omega_{base}}{\omega_e} \tag{22}$$

In order to guarantee that the back-EMF does not exceed tolerable levels in the whole load range, full-load condition is considered. Thus, (22) is rewritten as

$$\lambda_s^* = \lambda_s^{max} \cdot \frac{\omega_{mech_{base}}}{\omega_{mech}} \tag{23}$$

C. STATOR FLUX ESTIMATION

Theoretically, the stator flux could be determined by integrating the electromagnetic force of the motor by $\lambda_{\alpha\beta s} = \int \left(v_{\alpha\beta S} - R_s i_{\alpha\beta S} \right) dt$. However, the implementation of an integrator for motor flux estimation has dc drift and initial value problems. Even a small portion of this dc offset can drive a pure integrator into saturation [43]. In the literature, different methods based on the "voltage model" are used to
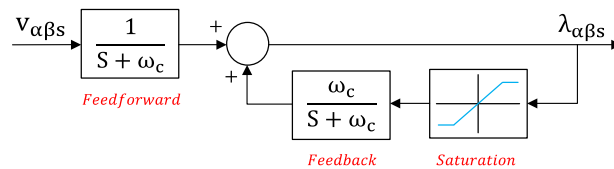
FIGURE 12. Modified integrator with saturable feedback.

modify the integrators and remove the dc drift problem. The method "Algorithm 1" proposed in [43] is implemented in this study. This method offers good results, easy implementation, and complete independence from motor parameters. The block diagram of this stator flux estimator is shown in Fig. 12.

Based on this algorithm, $\left|\overrightarrow{\lambda_s}\right|$ and θ_{λ_s} can be obtained by (24) and (25), respectively.

$$\left|\overrightarrow{\lambda_s}\right| = \sqrt{\left(\lambda_{\alpha s}^2 + \lambda_{\beta s}^2\right)} \tag{24}$$

$$\theta_{\lambda_s} = \tan^{-1}\left(\lambda_{\beta s}/\lambda_{\alpha s}\right) \tag{25}$$

VII. EXPERIMENTAL RESULTS AND DISCUSSIONS

To verify the performance of the method that we propose, experimental measurements were performed with motor parameters as presented in Table 3. Furthermore, its performance was compared with the conventional DTC as well as with the eighteen sectors DTC from [40]. Each algorithm was implemented on TMS320F280049 (32-bit, 100MHz) microcontroller from Texas Instruments. $t_{dead} = 2\mu s$, $U_{DC} = 600V$, $T_s = 25\mu s$, $\Delta T_{increase} = |\Delta T_{decrease}| = 0.1\text{Nm}/\text{s}$.

As is presented in Fig. 13(b), two IMs are connected through a coupling. One motor is used to implement either conventional DTC, eighteen sectors DTC or the proposed control algorithm while the other is controlled with conventional DTC as a load. Three-phase currents are measured using Hall effect sensors. An incremental encoder is used to measure the rotor speed. Fig. 13(a) shows the circuit prototype. It is composed of two three-phase inverters which share the same DC bus. In this fashion, the energy required to drive the motor is recycled by the load and returned to the DC bus. This configuration has two main advantages:

1) Only a small power supply to provide the energy dissipated by the losses is required.
2) No need for a resistor bank to dissipate the energy at the output of the load inverter.

Based on the parameters for the experimental setup where the proposed algorithm has been validated, Fig. 14 shows a graphical representation of (13), (16), and (19). For the case where $T < T^*$, $m = 1$ corresponds to $\omega_{mech_{base}} = 174\text{rad}/\text{sec}$. If ω_{mech} is further increased, m will be kept constant at $m = 1$, and the full $\overrightarrow{U_{actual}}$ will be applied to increase T. $\omega_{zero_{bound}} = 52\text{rad}/\text{sec}$. Hence, below this value, T is decreased by means of $\overrightarrow{U_Z}$, as it is explained in Fig. 10. For the case where $T > T^*$, the maximum value of m is equal to 0.65. It is obtained for $\omega_{mech} = \omega_{mech_{base}}$. If ω_{mech}

(a)

(b)

FIGURE 13. Prototype for experimental verification: (a) Circuit with the two inverters sharing the same DC bus; (b) Motor and load connected through a coupling.

is further increased, m will be reduced according to (19), as it is explained in section V. If FW is not implemented and $\lambda_s^* = \lambda_s^{max}$, the constant T region can be extended up to $\omega_{mech_{max}} = 202 \text{rad}/\text{sec}$.

A. STARTUP STAGE

In DTC, $\overrightarrow{\lambda_s}$ and T are directly controlled while the stator current is not directly regulated. If the IM is started directly without any special consideration on the current control, there may be a large starting current that triggers the over-current protection. Thus, to limit the starting current, $\left|\overrightarrow{\lambda_s}\right|$ should be first stabilized before applying any T. The process of machine magnetization is called pre-excitation. During this process, $\omega_{mech}^* = 0$ and λ_s^* is slowly increased.

Figure 15 shows the startup process of our proposed method. Fig. 15(a) presents the pre-excitation process and

TABLE 3. Parameters of the Induction Motor.

Parameter	Value	Parameter	Value
Rated Power	1.5 kW	Rated Torque	10 N·m
Rated Speed	1800 r/min	Stator Resistance	4.48 Ω
Rated Voltage	380 V	Rotor Resistance	2.78 Ω
Rated Current	3.3 A	Mutual Inductance	0.415 H
Rated Frequency	60 Hz	Stator Inductance	0.43 H
Inertia	0.017 kg·m²	Rotor Inductance	0.43 H
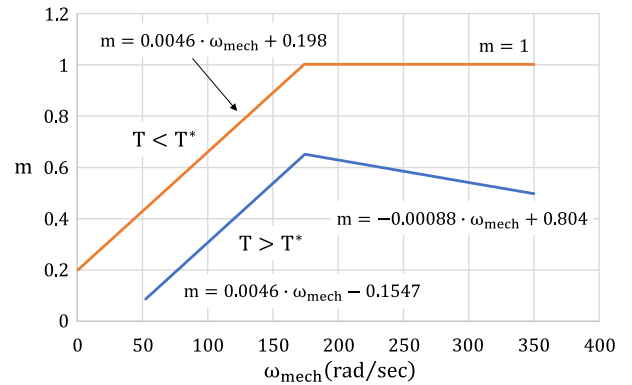
FIGURE 14. Relationship between m and the mechanical speed.

the acceleration process from $\omega_{mech}^* = 0 \text{rad}/\text{sec}$ to $\omega_{mech}^* = 40 \text{rad}/\text{sec}$. Equally, Fig. 15(b) presents the pre-excitation process and the acceleration process from $\omega_{mech}^* = 0 \text{rad}/\text{sec}$ to $\omega_{mech}^* = 170 \text{rad}/\text{sec}$.

The experimental results show that the pre-excitation process works properly. $\left|\overrightarrow{\lambda_s}\right|$ perfectly follows λ_s^* and the stator current is kept under minimum levels. Once the pre-excitation procedure is over, it can be seen that in both scenarios the acceleration process is notoriously smooth. ω_{mech} perfectly follows its command until steady-state operation is reached.

The results presented in Fig. 15(b) corroborate the theoretical analysis that took place regarding T_{ripp} reduction when $T > T^*$. It can be observed that while $\omega_{mech} < \omega_{zero_{bound}}$, T drop increases along with the speed increment. Once $\omega_{mech} > \omega_{zero_{bound}}$, our T_{ripp} minimization algorithm for the case where $T > T^*$ comes into action. After this point, T drop no longer increases with the speed. Thus, the effectiveness of our proposed method is proven.

B. MAXIMUM ATTAINABLE SPEED AND ACCELERATION PROCESS

In the same manner that it was done for the method that we propose, $\omega_{mech_{max}}$ is obtained for the eighteen sectors DTC. Hence, from Fig. 5, a graphical representation of $\overrightarrow{\lambda_s}$ when both T and $\left|\overrightarrow{\lambda_s}\right|$ have to be increased is summarized in Fig. 16(a). Equally, Fig. 16(b) illustrates the circumstance where T has to be increased but $\left|\overrightarrow{\lambda_s}\right|$, decreased.

According to the switching vector selection table of this method, depending on which sector $\overrightarrow{\lambda_s}$ is located, $\overrightarrow{U_{actual}}$
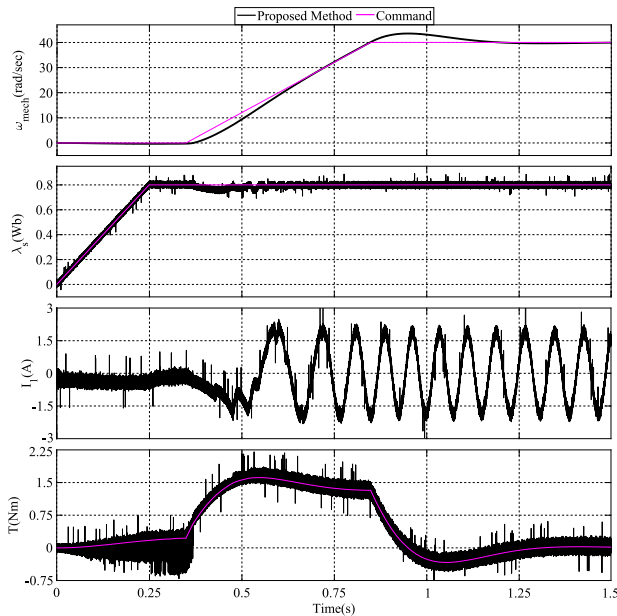
FIGURE 15. Startup stage: (a) from 0 to 40rad/sec; (b) from 0 to 170rad/sec.

or $\overrightarrow{U_{virtual}}$ can be selected. Hence, for Fig. 16(a), $\overrightarrow{U_A} = \overrightarrow{U_{virtual}} = \overrightarrow{U_2}$, if $\overrightarrow{\lambda_s}$ is in sector 1. However, $\overrightarrow{U_A} = \overrightarrow{U_{actual}} = \overrightarrow{U_4}$ if $\overrightarrow{\lambda_s}$ is in sector 3. Accordingly, for Fig. 16(b), $\overrightarrow{U_B} = \overrightarrow{U_{virtual}} = \overrightarrow{U_6}$, if $\overrightarrow{\lambda_s}$ is in sector 1. Nevertheless, $\overrightarrow{U_B} = \overrightarrow{U_{actual}} = \overrightarrow{U_7}$ if $\overrightarrow{\lambda_s}$ is in sector 2. Since $\cos(80°)/\cos(20°) \approx 0.185$, when T has to be increased, the situations depicted in Fig. 16(a)(b) are going to happen 18.5% and 81.5% of the time, respectively. Also, $\overrightarrow{U_{virtual}}$ and $\overrightarrow{U_{actual}}$ are going to be chosen 66.7% and 33.3% of the time, respectively. Thus, four different scenarios can be
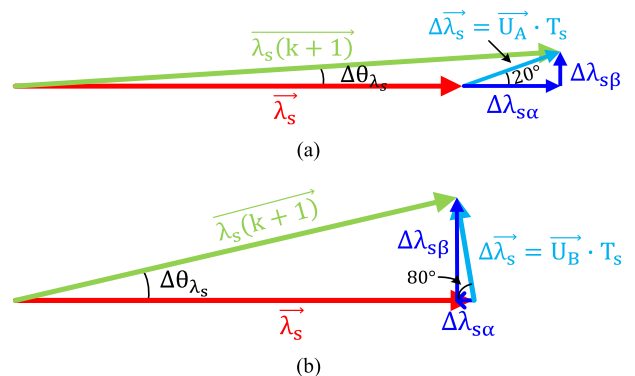
FIGURE 16. Stator flux vector when torque needs to be increased for the eighteen sectors DTC: (a) Stator flux module is increased; (b) Stator flux module is decreased.

found when T needs to be increased. Therefore, applying the same method described in (8)–(14), $\omega_{mech_{max}}$ for the eighteen sectors DTC can be obtained as the weighted average of these four situations.

$$\omega_{mech_{max}} = \frac{1}{P_P} \cdot \left(\frac{U_{DC}}{1.87 \cdot \lambda_s^*} - \omega_{sl_{max}} \right) \quad (26)$$

Figure 17 shows the comparison results of the step acceleration process at full load. It can be seen that for the conventional DTC and for the method that we propose $\omega_{mech_{max}} \approx 205$rad/sec. On the other hand, for the eighteen sectors DTC, $\omega_{mech_{max}} \approx 179$rad/sec. The importance of limiting T drop at high-speed is also proven in Fig. 17. It is shown how the proposed method effectively improves the acceleration response compared to the conventional DTC. The three algorithms show robustness to guarantee the flux controllability in the whole acceleration process. $\left| \overrightarrow{\lambda_s} \right|$ is kept within reasonable limits even when the T controllability is lost. I_1 degradation comes the earliest for the 18 sectors DTC as a result of the rapid loss of T production, which starts around 0.1s earlier than it does for the other two methods. The proposed algorithm shows a lower T_{ripp} in the whole acceleration process. The reason why T decreases slightly faster for the method that we propose than for the conventional DTC is that the acceleration process is faster, which means that $\omega_{mech_{max}}$, which being the same for both methods, is also reached faster.

Table 4 presents the theoretical and empirical results of $\omega_{mech_{max}}$ for the method that we propose and the eighteen sectors DTC.

The experimental results are very similar to the theoretical calculations, proving the accuracy of the equations developed in this paper. $\omega_{mech_{max}}$ is around 14.5% higher for the proposed method compared to the eighteen sectors DTC.

C. STEADY-STATE PERFORMANCE

The experimental results for steady-state conditions are presented for four different scenarios. Conventional DTC, eighteen sectors DTC, and the proposed method are compared. For the first scenario, $\omega_{mech}^* = 40$rad/sec and
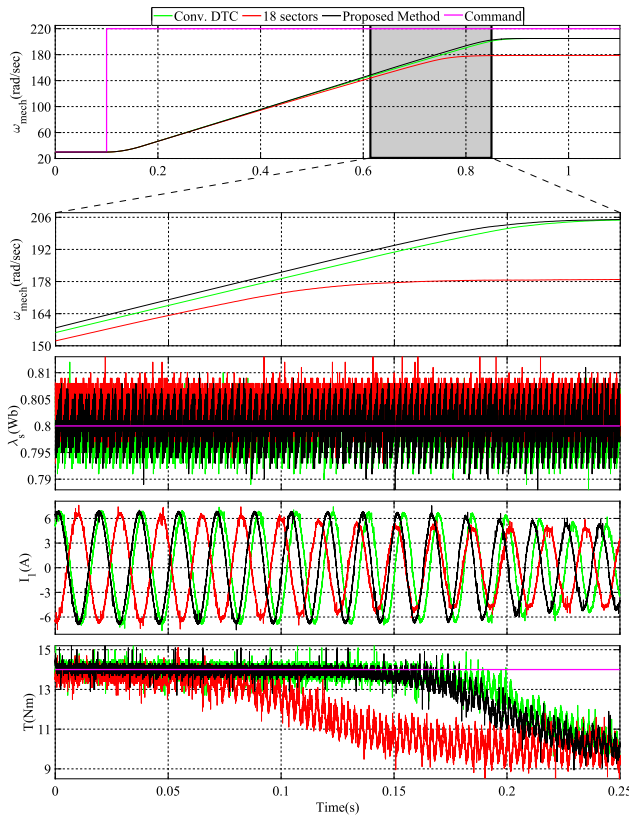
FIGURE 17. Maximum attainable speed and acceleration process comparison.

Method	Theoretical $\omega_{mech_{max}}$	Empirical $\omega_{mech_{max}}$
Proposed method	202 rad/sec	205 rad/sec
Eighteen sectors DTC	183 rad/sec	179 rad/sec

$T_{Load} = 1.5$Nm. For the second, $\omega^*_{mech} = 40$rad/sec and $T_{Load} = 10$Nm. For the third, $\omega^*_{mech} = 170$rad/sec and $T_{Load} = 1.5$Nm. For the fourth, $\omega^*_{mech} = 170$rad/sec and $T_{Load} = 10$Nm. Said conditions are presented in Fig. 18, Fig. 19, Fig. 20, and Fig. 21, respectively.

As is explained in Fig. 7 for conventional DTC and for the method that we propose, at the beginning of each sector, the $\overrightarrow{U_{actual}}$ selected when it is necessary to increase both T and $\left|\overrightarrow{\lambda_s}\right|$ is perpendicular to $\overrightarrow{\lambda_s}$. Hence, T production is maximum, but $\left|\overrightarrow{\lambda_s}\right|$ does not change. For the conditions presented in Fig. 18 and Fig. 19, both the proposed method and the conventional DTC rely on $\overrightarrow{U_Z}$ to reduce T. In this situation, as is explained in section III, T decreases very slowly when $\overrightarrow{U_Z}$ is applied. As a result, the number of cycles where $\overrightarrow{U_Z}$ is selected outstrips those where a non-zero voltage vector ($\overrightarrow{U_{actual}}$ for conventional DTC and $\overrightarrow{U_{active}}$ for the method that we propose) is selected. When $\overrightarrow{U_Z}$ is applied, $\overrightarrow{\lambda_s}$ is stopped. Due to the fact of the presence of R_s, $\left|\overrightarrow{\lambda_s}\right|$ decreases slightly as well. This is the reason behind the valleys that can be observed in the $\left|\overrightarrow{\lambda_s}\right|$ and I_1 waveforms of Fig. 18 and Fig 19. In these conditions, $\left|\overrightarrow{U_{actual}}\right| > \left|\overrightarrow{U_{active}}\right|$. Thus, the number of cycles where a non-zero voltage vector is chosen is higher for the method that we propose than for the conventional DTC. As a result, valleys are not as drastic as

for conventional DTC. The 18 sectors DTC does not provide any situation where $\overrightarrow{U_{virtual}}$ is perpendicular to $\overrightarrow{\lambda_s}$. In consequence, this method lacks the valleys that can be seen on the other two methods. Nevertheless, it is observed that the 18 sectors DTC tends to over increase $\left|\overrightarrow{\lambda_s}\right|$, producing an average value of $\left|\overrightarrow{\lambda_s}\right|$ higher than λ^*_s. In addition, despite not having the valleys that the method we propose has, the peak-to-peak value of $\left|\overrightarrow{\lambda_s}\right|$ is slightly higher for the 18 sectors DTC. The effectiveness of the method that we propose to reduce T_{ripp} in the low-speed region is proven in Fig. 18 and Fig. 19.

In contrast to what happens in the low-speed region presented in Fig. 18 and Fig 19, for the high-speed region shown in Fig. 20 and Fig. 21, the number of cycles where $T < T^*$ outstrips those where $T > T^*$. Additionally, the effect of R_s is less determinant in the high-speed region. As a result, the valleys on $\left|\overrightarrow{\lambda_s}\right|$ and I_1 that appeared for the low-speed region, do not appear for the high-speed region. For $\omega^*_{mech} = 170$rad/sec it happens that for the method that we propose, $\left|\overrightarrow{U_{active}}\right| \approx \left|\overrightarrow{U_{actual}}\right|$ when $T < T^*$ and $\left|\overrightarrow{U_{active}}\right| = 0.63 \cdot \left|\overrightarrow{U_{actual}}\right|$ when $T > T^*$. Hence, it is evident that for the conditions shown in Fig. 20 and Fig. 21, T_{ripp} reduction mainly takes place for the case where $T > T^*$. Since T_{ripp} is greatly reduced compared to the other two methods, it proves the importance of limiting T drop and not applying $\overrightarrow{U_Z}$ in the high-speed region.

From the experimental results, it can be observed that the method we propose significantly reduces T_{ripp} and current distortion for every situation presented above. As it is stated in [39], the current THD is mainly influenced by T_{ripp}. $\left|\overrightarrow{\lambda_s}\right|$ ripple has a small influence on said THD.

D. SWITCHING FREQUENCY, T_{ripp} AND COMPUTATIONAL BURDEN COMPARISON

Figure 22 shows a T_{ripp} comparison for the method that we propose, conventional DTC, and eighteen sectors DTC. T_{ripp} is calculated within one full current (I_1) cycle. $T_{ripp} = 100 \cdot (T_{max} - T_{min}) / T_{avg}$.

The experimental results presented in Fig. 22 show that a significant T_{ripp} reduction is achieved in all conditions. Especially, at light-load and low-speed, where T_{ripp} is reduced by almost 40%. The proposed algorithm has been proved to be much more effective to minimize T_{ripp} than the 18 sectors DTC. Furthermore, in the high-speed region, 18 sectors DTC shows a higher T_{ripp} than the conventional DTC. Since $\omega_{mech_{max}} = 179$rad/sec for the 18 sectors DTC,

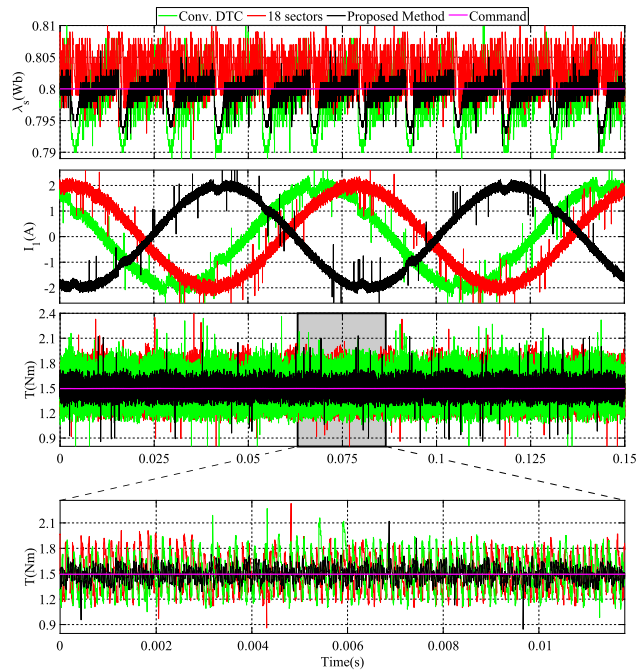**FIGURE 18.** Steady-state performance comparison for low-speed and light-load conditions.
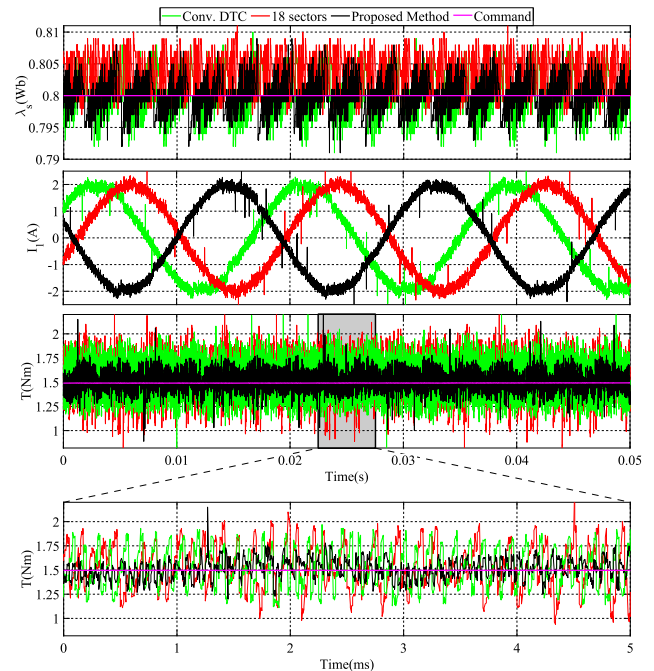

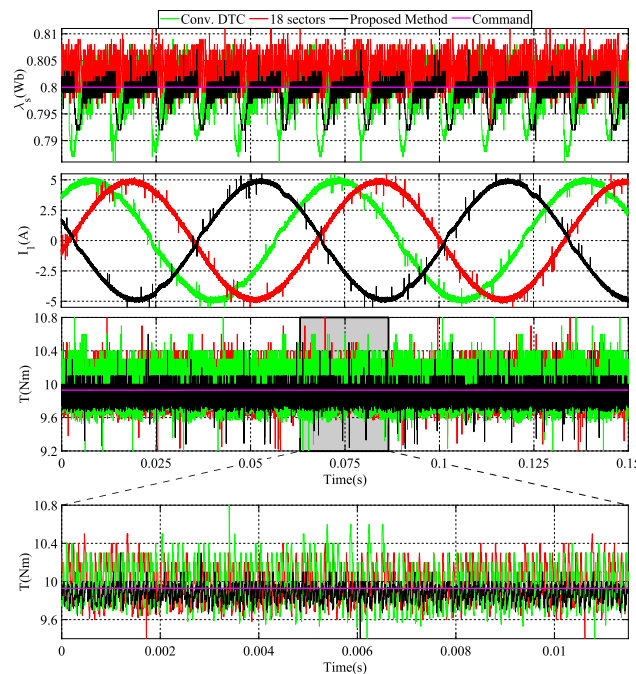**FIGURE 20.** Steady-state performance comparison for high-speed and low-load conditions.

FIGURE 19. Steady-state performance comparison for low-speed and full-load conditions.
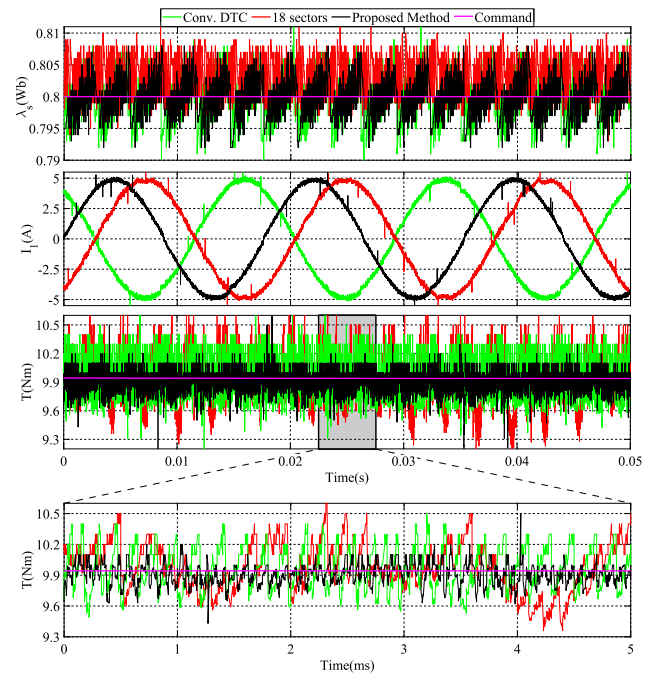

FIGURE 21. Steady-state performance comparison for high-speed and full-load conditions.

Fig. 22 only presents T_{ripp} results for this method up to $\omega_{mech} = 170 \text{rad}/\text{sec}$.

In order to demonstrate the effectiveness of the method that we proposed in terms of T_{ripp} reduction, Fig. 22 also shows the T_{ripp} results for the proposed algorithm with a sampling frequency of 20kHz ($T_s = 50\mu s$). It can be observed that even

though T_s is twice as long as for both conventional DTC and eighteen sectors DTC, T_{ripp} is smaller in every circumstance.

The average switching frequency (F_{sw}) comparison for the method that we propose, conventional DTC and eighteen sectors DTC is presented in Fig. 23. It can be seen that when the proposed method is implemented with a $T_s = 25\mu s$,
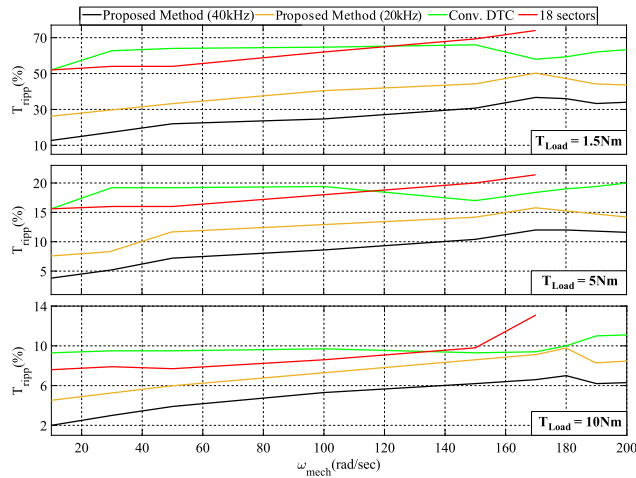
FIGURE 22. Torque ripple comparison.
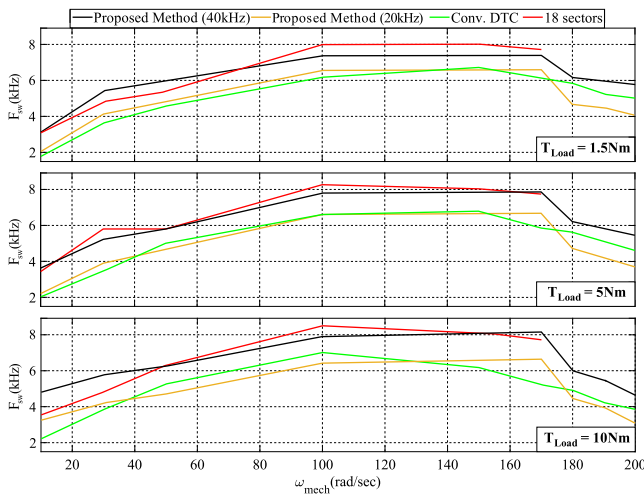
FIGURE 23. Switching frequency comparison.

its F_{sw} is similar to that of eighteen sectors DTC. On the other hand, when the proposed method is implemented with a $T_s = 50\mu s$, its F_{sw} is similar to that of conventional DTC.

The high-speed regions of Fig. 22 and Fig. 23 show how applying $\overrightarrow{U_{active}}$ instead of $\overrightarrow{U_Z}$ when $T > T^*$ has little impact on F_{sw} but great impact on T_{ripp} reduction. It is noticeable that in this speed region, when $m = 1$ for the case where $T < T^*$, F_{sw} is just slightly higher for the proposed method compared to the conventional DTC. However, when the proposed method is implemented with a $T_s = 50\mu s$, F_{sw} is smaller than for the conventional DTC.

The computational burden has been tested by measuring the required execution time on the TMS320F280049. Table 5 shows the computing time for the proposed method, eighteen sectors DTC and conventional DTC. The proposed method and eighteen sectors DTC require a similar computational time, which is only slightly longer than for conventional DTC. Nevertheless, since the proposed method offers a smaller T_{ripp} even for $T_s = 50\mu s$, it can be stated that the

TABLE 5. Computing Time Comparison.

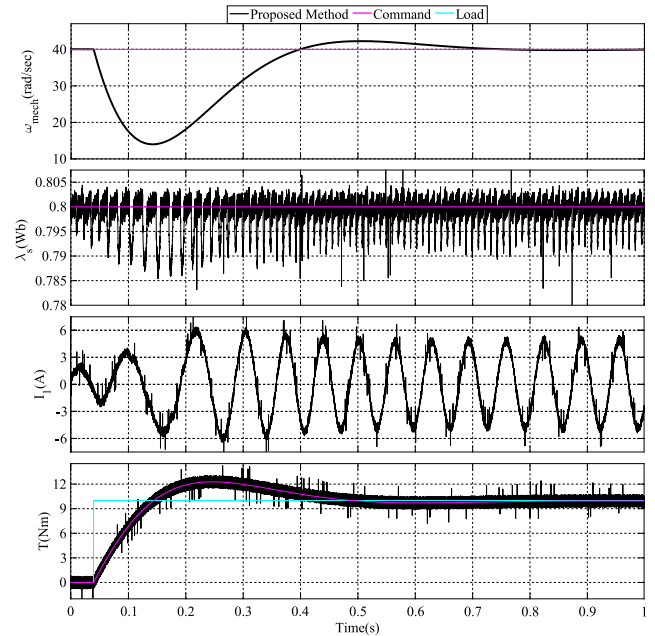| Control Method	Computing Time (μs)
Proposed method	18.2
Eighteen sectors DTC	18
Conventional DTC	14.9

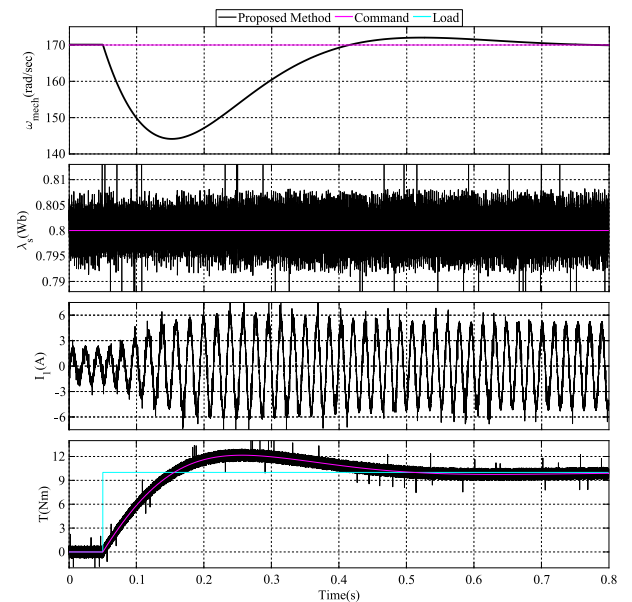**FIGURE 24.** Step load response at low-speed.

FIGURE 25. Step load response at high-speed.

computational burden on the controller is smaller than for eighteen sectors DTC and conventional DTC.

From the experimental results, it is proven that at equal F_{sw}, the proposed method presents a smaller T_{ripp} and
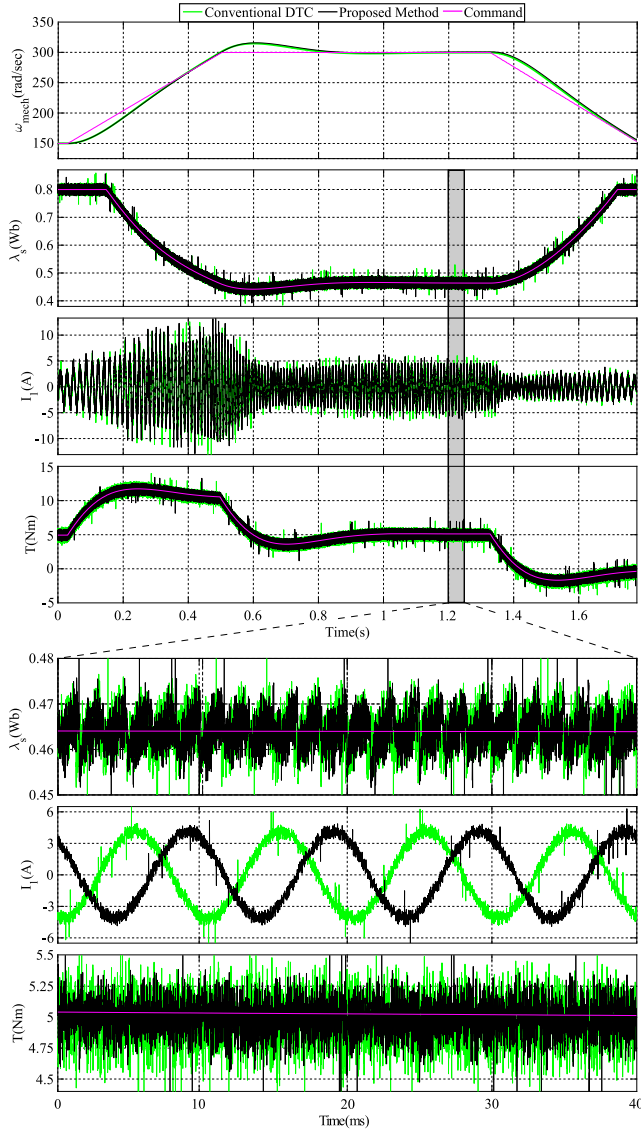
FIGURE 26. Flux weakening operation.

computational burden than the eighteen sectors DTC and conventional DTC in all conditions.

E. STEP LOAD RESPONSE

In order to show the step load response of the proposed method, Fig.24 and Fig.25 present the experimental results for a step on the load from $T_{Load} = 0$Nm to $T_{Load} = 10$Nm at constant speed. Fig. 24 shows the results for $\omega^*_{mech} = 40$rad/sec and Fig. 25 for $\omega^*_{mech} = 170$rad/sec.

As it was explained for Fig. 18 and Fig. 19, some valleys can be observed in $\left| \overrightarrow{\lambda_s} \right|$ the in the low-speed region of Fig. 24. However, despite having some valleys in this region, the maximum $\left| \overrightarrow{\lambda_s} \right|$ drop that can be seen in Fig. 24 is around 1.8%. This value is obtained for $\omega_{mech} \approx 15$rad/sec. Thus, an indubitably stable $\left| \overrightarrow{\lambda_s} \right|$ is obtained even in the very low-speed region. In the two situations presented in Fig. 24 and

Fig. 25, it is clear that T perfectly follows T^* until the steady-state region is reached. The T production is very steady in the whole load region, at the same time that T_{ripp} is kept under minimum levels.

F. FLUX WEAKENING REGION

In order to prove its versatility, the proposed method is extended to the high-speed region above $\omega_{mech_{base}}$ by introducing the FW method described in sections V and VI. Fig. 26 presents the acceleration and deceleration process from $\omega^*_{mech} = 150$rad/sec to $\omega^*_{mech} = 300$rad/sec and back to $\omega^*_{mech} = 150$rad/sec for $T_{Load} = 5$Nm. In this figure, the method that we propose is compared with the conventional DTC. It can be seen that when $\omega_{mech} > \omega_{mech_{base}} = 174$rad/sec, $\lambda^*_s \neq \lambda^{max}_s = 0.8$Wb. Instead, λ^*_s is generated according to (23).

In this region, both our method and the conventional DTC increase T by applying the whole $\overrightarrow{U_{actual}}$. On the other hand, the approach to reduce T is different between these control methods. The conventional DTC reduces T by means of applying $\overrightarrow{U_Z}$. However, our method reduces T by applying $\overrightarrow{U_{active}}$, which is modulated according to (19).

It can be observed that our method exhibits a smaller T_{ripp} in the whole FW process compared to the conventional DTC. Thus, the effectiveness of the proposed method to limit T drop applying (19) when $T > T^*$ in the FW region is proven.

A very stable behavior of both T and $\left| \overrightarrow{\lambda_s} \right|$ is found in the whole FW region, where these two magnitudes perfectly follow their respective command.

VIII. CONCLUSION

This paper focuses on the T_{ripp} reduction of DTC-based algorithms. T_{ripp} sources at low and high-speed regions are analyzed. From this analysis, a novel DTC algorithm to minimize T_{ripp} while preserving the conventional DTC strengths is presented in this article. The feasibility of the prosed scheme in the constant T and in the FW regions is verified by means of experimental analysis. The results showed that a great T_{ripp} reduction was achieved with smaller F_{sw} and computational burden than both the conventional DTC and eighteen sectors DTC. Furthermore, all the positive attributes of the conventional DTC were preserved. Moreover, limiting T drop at high-speed is also proven to improve the acceleration response compared to the conventional DTC.

REFERENCES

[1] B. K. Bose, *Modern Power Electronics and AC Drives*. Englewood Cliffs, NJ, USA: Prentice-Hall, 2002.

[2] B. Wu, *High-Power Converters and AC Drives*. Hoboken, NJ, USA: Wiley, 2007.

[3] S. Suresh and P. P. Rajeevan, "Virtual space vector based direct torque control schemes for induction motor drives," in *Proc. 8th IEEE India Int. Conf. Power Electron. (IICPE)*, Dec. 2018, pp. 1–6, doi: 10.1109/IICPE.2018.8709454.

[4] I. Takahashi and T. Noguchi, "A new quick-response and high-efficiency control strategy of an induction motor," *IEEE Trans. Ind. Appl.*, vol. IA-22, no. 5, pp. 820–827, Sep. 1986, doi: 10.1109/TIA.1986.4504799.

[5] G. S. Buja and M. P. Kazmierkowski, "Direct torque control of PWM inverter-fed AC motors—A survey," *IEEE Trans. Ind. Electron.*, vol. 51, no. 4, pp. 744–757, Aug. 2004, doi: 10.1109/TIE.2004.831717.

[6] Z. Wang, J. Chen, M. Cheng, and K. T. Chau, "Field-oriented control and direct torque control for paralleled VSIs fed PMSM drives with variable switching frequencies," *IEEE Trans. Power Electron.*, vol. 31, no. 3, pp. 2417–2428, Mar. 2016, doi: 10.1109/TPEL.2015.2437893

[7] R. Ortega, N. Barabanov, G. Escobar, and E. Valderrama, "Direct torque control of induction motors: Stability analysis and performance improvement," *IEEE Trans. Autom. Control*, vol. 46, no. 8, pp. 1209–1222, Aug. 2001, doi: 10.1109/9.940925.

[8] C. Patel, R. P. P. A. Day, A. Dey, R. Ramchand, K. Gopakumar, and M. P. Kazmierkowski, "Fast direct torque control of an open-end induction motor drive using 12-sided polygonal voltage space vectors," *IEEE Trans. Power Electron.*, vol. 27, no. 1, pp. 400–410, Jan. 2012, doi: 10.1109/TPEL.2011.2159516.

[9] T. G. Habetler, F. Profumo, M. Pastorelli, and L. M. Tolbert, "Direct torque control of induction machines using space vector modulation," *IEEE Trans. Ind. Appl.*, vol. 28, no. 5, pp. 1045–1053, Sep. 1992, doi: 10.1109/28.158828.

[10] Z. Zhang, R. Tang, B. Bai, and D. Xie, "Novel direct torque control based on space vector modulation with adaptive stator flux observer for induction motors," *IEEE Trans. Magn.*, vol. 46, no. 8, pp. 3133–3136, Aug. 2010, doi: 10.1109/TMAG.2010.2051142.

[11] C. Lascu, S. Jafarzadeh, M. S. Fadali, and F. Blaabjerg, "Direct torque control with feedback linearization for induction motor drives," *IEEE Trans. Power Electron.*, vol. 32, no. 3, pp. 2072–2080, Mar. 2017, doi: 10.1109/TPEL.2016.2564943.

[12] E. Ozkop and H. I. Okumus, "Direct torque control of induction motor using space vector modulation (SVM-DTC)," in *Proc. 12th Int. Middle-East Power Syst. Conf.*, Mar. 2008, pp. 368–372, doi: 10.1109/MEP-CON.2008.4562350.

[13] H. I. Okumus and M. Aktas, "Direct torque control of induction machine drives using adaptive hysteresis band for constant switching frequency," in *Proc. IEEE Int. Electric Mach. Drives Conf.*, May 2007, pp. 1762–1767, doi: 10.1109/IEMDC.2007.383697.

[14] S. Srivastava and A. K. Jain, "High performance constant switching frequency hysteresis-based direct torque control technique," in *Proc. IEEE Int. Conf. Power Electron., Drives Energy Syst. (PEDES)*, Dec. 2014, pp. 1–5, doi: 10.1109/PEDES.2014.7042067.

[15] K.-B. Lee, J.-H. Song, I. Choy, and J.-Y. Yoo, "Torque ripple reduction in DTC of induction motor driven by three-level inverter with low switching frequency," *IEEE Trans. Power Electron.*, vol. 17, no. 2, pp. 255–264, Mar. 2002, doi: 10.1109/63.988836.

[16] V. Naik N and S. P. Singh, "A novel interval type-2 fuzzy-based direct torque control of induction motor drive using five-level diode-clamped inverter," *IEEE Trans. Ind. Electron.*, vol. 68, no. 1, pp. 149–159, Jan. 2021, doi: 10.1109/TIE.2019.2960738.

[17] D. Mohan, X. Zhang, and G. H. B. Foo, "A simple duty cycle control strategy to reduce torque ripples and improve low-speed performance of a three-level inverter fed DTC IPMSM drive," *IEEE Trans. Ind. Electron.*, vol. 64, no. 4, pp. 2709–2721, Apr. 2017, doi: 10.1109/TIE.2016.2636202.

[18] R. E. Kodumur Meesala and V. K. Thippiripati, "An improved direct torque control of three-level dual inverter fed open-ended winding induction motor drive based on modified look-up table," *IEEE Trans. Power Electron.*, vol. 35, no. 4, pp. 3906–3917, Apr. 2020, doi: 10.1109/TPEL.2019.2937684.

[19] N. K. Bajjuri and A. K. Jain, "An improved dual DTC of double-inverter-fed WRIM drive with reduced torque ripple by emulating equivalent 3L NPC VSC," *IEEE Trans. Ind. Electron.*, vol. 69, no. 6, pp. 5453–5464, Jun. 2022, doi: 10.1109/TIE.2021.3088379.

[20] B. R. Vinod and G. Shiny, "Direct torque control scheme for a four-level-inverter fed open-end-winding induction motor," *IEEE Trans. Energy Convers.*, vol. 34, no. 4, pp. 2209–2217, Dec. 2019, doi: 10.1109/TEC.2019.2941890.

[21] P. Naganathan and S. Srinivas, "Direct torque control techniques of three-level H-bridge inverter fed induction motor for torque ripple reduction at low speed operations," *IEEE Trans. Ind. Electron.*, vol. 67, no. 10, pp. 8262–8270, Oct. 2020, doi: 10.1109/TIE.2019.2950840.

[22] D. Mohan, X. Zhang, and G. H. B. Foo, "Generalized DTC strategy for multilevel inverter fed IPMSMs with constant inverter switching frequency and reduced torque ripples," *IEEE Trans. Energy Convers.*, vol. 32, no. 3, pp. 1031–1041, Sep. 2017, doi: 10.1109/TEC.2017.2681653.

[23] S. S. Hakami, I. M. Alsofyani, and K.-B. Lee, "Torque ripple reduction and flux-droop minimization of DTC with improved interleaving CSFTC of IM fed by three-level NPC inverter," *IEEE Access*, vol. 7, pp. 184266–184275, 2019, doi: 10.1109/ACCESS.2019.2960685.

[24] X. Wu, W. Huang, Y. Zhao, and C. Huang, "An efficient model predictive torque control for induction motors with flexible duty ratio optimization," *IEEE J. Emerg. Sel. Topics Power Electron.*, vol. 10, no. 4, pp. 4014–4025, Aug. 2022, doi: 10.1109/JESTPE.2021.3100920.

[25] M. R. Nikzad, B. Asaei, and S. O. Ahmadi, "Discrete duty-cycle-control method for direct torque control of induction motor drives with model predictive solution," *IEEE Trans. Power Electron.*, vol. 33, no. 3, pp. 2317–2329, Mar. 2018, doi: 10.1109/TPEL.2017.2690304.

[26] A. Berzoy, O. Mohammed, and J. Rengifo, "Fuzzy predictive DTC of induction machines with reduced torque ripple and high-performance operation," *IEEE Trans. Power Electron.*, vol. 33, no. 3, pp. 2580–2587, Mar. 2018, doi: 10.1109/TPEL.2017.2690405.

[27] C. Martín, M. Bermúdez, F. Barrero, M. R. Arahal, X. Kestelyn, and M. J. Durán, "Sensitivity of predictive controllers to parameter variation in five-phase induction motor drives," *Control Eng. Pract.*, vol. 68, pp. 23–31, Nov. 2017.

[28] M. Vatani, B. Bahrani, M. Saeedifard, and M. Hovd, "Indirect finite control set model predictive control of modular multilevel converters," *IEEE Trans. Smart Grid*, vol. 6, no. 3, pp. 1520–1529, May 2015, doi: 10.1109/TSG.2014.2377112.

[29] X. Zhang, B. Hou, and Y. Mei, "Deadbeat predictive current control of permanent-magnet synchronous motors with stator current and disturbance observer," *IEEE Trans. Power Electron.*, vol. 32, no. 5, pp. 3818–3834, May 2017, doi: 10.1109/TPEL.2016.2592534.

[30] J. A. Riveros, A. G. Yepes, F. Barrero, J. Doval-Gandoy, and B. Bogado, "Parameter identification of multiphase induction machines with distributed windings—Part 2: Time-domain techniques," *IEEE Trans. Energy Conv.*, vol. 27, no. 4, pp. 1067–1077, Aug. 2012, doi: 10.1109/TEC.2012.2219862.

[31] H. A. Young, A. Perez, and J. Rodriguez, "Analysis of finite-control-set model predictive current control with model parameter mismatch in a three-phase inverter," *IEEE Trans. Ind. Electron.*, vol. 63, no. 5, pp. 3100–3107, May 2016, doi: 10.1109/TIE.2016.2515072.

[32] F. Morel, X. Lin-Shi, J.-M. Retif, B. Allard, and C. Buttay, "A comparative study of predictive current control schemes for a permanent-magnet synchronous machine drive," *IEEE Trans. Ind. Electron.*, vol. 56, no. 7, pp. 2715–2728, Jul. 2009, doi: 10.1109/TIE.2009.2018429.

[33] M. Siami, D. A. Khaburi, A. Abbaszadeh, and J. Rodríguez, "Robustness improvement of predictive current control using prediction error correction for permanent-magnet synchronous machines," *IEEE Trans. Ind. Electron.*, vol. 63, no. 6, pp. 3458–3466, Jun. 2016, doi: 10.1109/TIE.2016.2521734.

[34] C. Xia, M. Wang, Z. Song, and T. Liu, "Robust model predictive current control of three-phase voltage source PWM rectifier with online disturbance observation," *IEEE Trans. Ind. Informat.*, vol. 8, no. 3, pp. 459–471, Aug. 2012, doi: 10.1109/TII.2012.2187912.

[35] P. Cortes, J. Rodriguez, C. Silva, and A. Flores, "Delay compensation in model predictive current control of a three-phase inverter," *IEEE Trans. Ind. Electron.*, vol. 59, no. 2, pp. 1323–1325, Feb. 2012, doi: 10.1109/TIE.2011.2157284.

[36] J.-K. Kang and S.-K. Sul, "New direct torque control of induction motor for minimum torque ripple and constant switching frequency," *IEEE Trans. Ind. Appl.*, vol. 35, no. 5, pp. 1076–1082, Sep. 1999, doi: 10.1109/28.793368.

[37] Z. Zhang and X. Liu, "A duty ratio control strategy to reduce both torque and flux ripples of DTC for permanent magnet synchronous machines," *IEEE Access*, vol. 7, pp. 11820–11828, 2019, doi: 10.1109/ACCESS.2019.2892121.

[38] S. G. Petkar and V. K. Thippiripati, "A novel duty-controlled DTC of a surface PMSM drive with reduced torque and flux ripples," *IEEE Trans. Ind. Electron.*, vol. 70, no. 4, pp. 3373–3383, Apr. 2023, doi: 10.1109/TIE.2022.3181405.

[39] D. Casadei, G. Grandi, G. Serra, and A. Tani, "Effects of flux and torque hysteresis band amplitude in direct torque control of induction machines," in *Proc. 20th Annu. Conf. IEEE Ind. Electron. (IECON)*, vol. 1, Sep. 1994, pp. 299–304, doi: 10.1109/IECON.1994.397792.

[40] S. Suresh and P. P. Rajeevan, "Virtual space vector-based direct torque control schemes for induction motor drives," *IEEE Trans. Ind. Appl.*, vol. 56, no. 3, pp. 2719–2728, May 2020, doi: 10.1109/TIA.2020.2978447.

[41] P. Vas, *Sensorless Vector and Direct Torque Control*. Oxford, NY, USA: Oxford Univ. Press, 1998.

[42] T. Esparza Sola, H.-J. Chiu, Y.-C. Liu, and A. N. Rahman, "Extending DC bus utilization for induction motors with stator flux oriented direct torque control," *Energies*, vol. 15, no. 1, p. 374, Jan. 2022, doi: 10.3390/en15010374.

[43] J. Hu and B. Wu, "New integration algorithms for estimating motor flux over a wide speed range," *IEEE Trans. Power Electron.*, vol. 13, no. 5, pp. 969–977, Sep. 1998, doi: 10.1109/63.712323.

[44] X. Sun, Y. Xiong, J. Yang, and X. Tian, "Torque ripple reduction for a 12/8 switched reluctance motor based on a novel sliding mode control strategy," *IEEE Trans. Transp. Electrific.*, early access, Mar. 21, 2022, doi: 10.1109/TTE.2022.3161078.

[45] R. De Doncker, D. W. J. Pulle, and A. Veltman, *Advanced Electrical Drives: Analysis, Modeling, Control*, 2nd ed. Berlin, Germany: Springer, 2020.

[46] L. Feng, X. Sun, X. Tian, and K. Diao, "Direct torque control with variable flux for an SRM based on hybrid optimization algorithm," *IEEE Trans. Power Electron.*, vol. 37, no. 6, pp. 6688–6697, Jun. 2022, doi: 10.1109/TPEL.2022.3145873.

[47] D. Casadei, M. Mengoni, G. Serra, A. Tani, and L. Zarri, "A control scheme with energy saving and DC-link overvoltage rejection for induction motor drives of electric vehicles," *IEEE Trans. Ind. Appl.*, vol. 46, no. 4, pp. 1436–1446, Jul. 2010, doi: 10.1109/TIA.2010.2049627.

HUANG JEN CHIU (Senior Member, IEEE) was born in Ilan, Taiwan, in 1971. He received the B.E. and Ph.D. degrees in electronic engineering from the National Taiwan University of Science and Technology (NTUST), Taipei, Taiwan, in 1996 and 2000, respectively. He is currently a Distinguished Professor and the Director of the Center for Power Electronic Technologies, Department of Electronic and Computer Engineering, NTUST, where he is also the Dean of Industry–Academia Collaboration. He is also a fellow of the Institute of Engineering and Technology (IET). He was a recipient of several distinctive awards, including the Young Researcher Award from the Ministry of Science and Technology, Taiwan, in 2004; the Outstanding Teaching Awards from NTUST, in 2009 and 2017; the Excellent Research Award from NTUST, in 2009 and 2011; the Y. Z. Hsu Scientific Paper Award, in 2010; the Excellent Industry–Academia Collaboration Award, in 2015 and 2017; the Outstanding Industry–Academia Collaboration Award, in 2018; and Google Little Box Academic Awards. His student teams won the grand prize of the IEEE International Future Energy Challenge (IFEC), in 2013 and 2015, respectively, and the IEEE Empower a Billion Lives (EBL) Pacific Asia Regional Award, in 2018. He was the Chair of IEEE Industrial Electronics Society Taipei Chapter, from 2015 to 2016, the General Co-Chair of 2017 IEEE International Future Energy Electronics Conference (IFEEC 2017–ECCE Asia), the Program Chair of 2015 IEEE International Future Energy Electronics Conference (IEEE IFEEC 2015), the Topic Co-Chair of 2016 International Future Energy Challenge (IFEC 2016), and the Secretary of IEEE PELS/IES Taipei Joint Chapter, from 2010 to 2014. He is also an Associate Editor of the IEEE Transactions on Industry Applications and IEEE Transactions on Circuits and Systems—Part II: Express Briefs. He was a Distinguished Lecturer of the IEEE Power Electronics Society, from 2017 to 2018 and from 2019 to 2020.

YU-CHEN LIU (Senior Member, IEEE) received the M.S. and Ph.D. degrees in electronic and computer engineering from the National Taiwan University of Science and Technology (NTUST), Taipei, Taiwan, in 2009 and 2015, respectively. He was a Visiting Researcher with the Future Energy Electronics Center, Virginia Tech, Blacksburg, VA, USA, in 2014. From 2015 to 2016, he was a Research Assistant Professor with the Power Electronics Laboratory, Department of Electronic Engineering, NTUST. He is currently an Assistant Professor with the Department of Electrical Engineering, National Ilan University, Yilan, Taiwan. He was a recipient the Young Researcher Award from the National Science Council of Taiwan, in 2018. He was a Faculty Advisor of Student Teams of the IEEE International Future Energy Challenge, receiving awards, in 2015, 2016, and 2017. He was the Chair of the IEEE Industrial Applications Society Taipei Chapter during 2017–2018.

TOMAS ESPARZA SOLA was born in Pamplona, Spain, in 1993. He received the B.Sc. and M.Sc. degrees in electrical engineering from the Public University of Navarre, Pamplona, in 2015 and 2017, respectively. He is currently pursuing the Ph.D. degree with the Center for Power Electronic Technologies, National Taiwan University of Science and Technology, Taipei, Taiwan. He did his master's thesis at the National Dong Hwa University, Hualien, Taiwan, on the topic of advanced control for motor drives. During the year 2018, he was with the Photovoltaic Inverters Division, YSD Technology Company Ltd., Tainan, Taiwan, where he was a Research and Development Engineer. His current research interests include power electronics, direct torque control, field weakening, overmodulation, and parameter identification of induction motors and permanent magnet synchronous motors.

ARIEF NOOR RAHMAN was born in Yogyakarta, Indonesia, in 1992. He received the B.Eng. degree from Universitas Indonesia, Indonesia, in 2013, and the M.Sc. and Ph.D. degrees from the Department of Electronics and Computer Engineering, National Taiwan University of Science and Technology (NTUST), Taiwan, in 2015 and 2021, respectively. He is currently with Pegatron, Taiwan, where he is a Technical Manager. His research interests include three-phase VSCs, electric motor drives, wireless power transfer, and device characterizations.

● ● ●